Journal of Materials Chemistry A

Accepted Manuscript

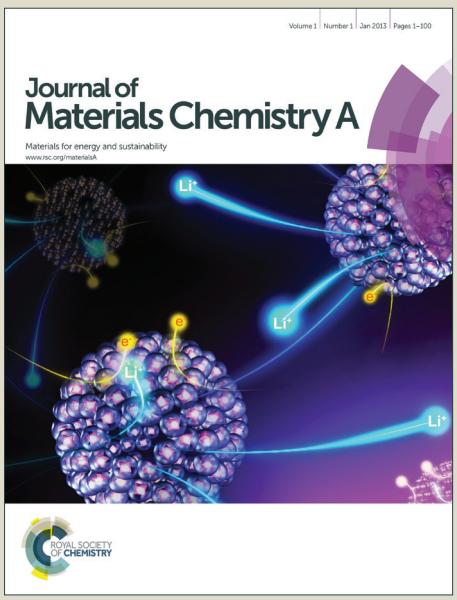

ROYAL SOCIETY OF CHEMISTRY

www.rsc.org/materialsA

Electric Double Layer Capacitors of High Volumetric Energy Based on Ionic Liquids and Hierarchical-Pore Carbon

Hsin-Chieh Huang,[1] Cheng-Wei Huang,[2] Chien-Te Hsieh,[3] Hsisheng Teng[1,4,*]

[1]Department of Chemical Engineering and Research Center for Energy Technology and Strategy, National Cheng Kung University, Tainan 70101, Taiwan

[2]Taiwan Textile Research Institute, Taipei 23674, Taiwan

[3]Department of Chemical Engineering and Materials Science, Yuan Ze Fuel Cell Center, Yuan Ze University, Taoyuan 32023, Taiwan

[4]Center for Micro/Nano Science and Technology, National Cheng Kung University, Tainan 70101, Taiwan

*To whom correspondenec should be addressed. E-mail: hteng@mail.ncku.edu.tw, Tel: 886-6-2385371, Fax:886-6-2344496

Abstract

In this study, we analyzes the high-voltage charge-storage behavior of electric double-layer capacitors in which two ionic-liquid electrolytes are used, 1-ethyl-3-methylimidazolium and 1-methyl-1-propylpyrrolidinium bis(trifluoromethylsulfonyl)imides (EMIm- and MPPy-TFSIs), and are operated at 3.5 and 4.1 V, respectively. Symmetric two-electrode capacitor cells assembled using micropore-rich activated mesophase pitch (aMP) and activated carbon fiber (aCF) carbons show a standard capacitive behavior in cyclic voltammetry analysis, whereas cells featuring templated mesoporous carbon (tMC) show ion-intercalating peaks in high-voltage scans. Impedance analysis performed at high voltages reveals that the aMP and aCF cells show lower charge-storage resistance than the tMC, although tMC facilitates ion transport more efficiently than aMP and aCF. The experimental results indicate that micropore-rich aMP and aCF accommodate single ions at high voltages, whereas the carbon structure is destroyed in micropore-deficient tMC because of graphitic-layer intercalation. The aMP carbon, which contains hierarchically connected micropores and mesopores, is effective in storing charge at a high rate at high voltages. Because of the compact feature of aMP, incorporating ionic liquids with aMP represents a very promising strategy for assembling capacitors of ultrahigh volumetric energy densities.

Keywords: Electric double-layer capacitor; Activated carbon; Porous carbon; Ionic liquid; Pore structure

1. Introduction

Electric double-layer capacitors (EDLCs) that store a substantial amount of charge on carbon electrodes exhibit a considerably higher power rating and cycling performance than do rechargeable batteries or fuel cells.[1–4] EDLCs are being increasingly used in numerous applications as complementary energy-storage parts to satisfy power requirements.[5] One of the major technological aims in developing EDLCs is to increase their energy density without sacrificing the high power characteristics. Selecting an appropriate electrolyte system for use in EDLCs represents an effective method to achieve this goal.[6,7] Traditional aqueous or organic electrolytes containing water or organic solvents exhibit limited operating voltage windows of approximately 1 or 2.5 V, respectively.[8–11] Solvent-free room-temperature ionic liquids (ILs) that exhibit wide voltage windows of electrochemical charge–discharge represent a highly suitable type of electrolyte for use in EDLCs.[12–18] These ILs, which are composed of asymmetric organic cations and anions and behave like molten salts or fused salts at room or lower temperatures, require no voltage-limiting solvents in charge transportation. However, the compatibility between ILs and carbon electrodes, which greatly influences the stability of EDLCs operated at high voltages, warrants in-depth scrutiny.

Room-temperature ILs are molecular liquids that feature numerous advantageous properties including high safety, negligible vapor pressure, non-flammability, high chemical and thermal stability (from −81 to +230 °C), a wide electrochemical stability window (>3 V), sufficient electrical conductivity (1–10 mS cm^{-1}), and a solvent-free "green" feature.[13,19–24] The most widely studied ILs for EDLC application are imidazolium and pyrrolidinium salts (see examples shown in Fig. S1 of the ESI†).

Imidazolium salts typically display the highest conductivities, whereas pyrrolidinium salts feature the widest electrochemical stability window.[13,20,25,26] When considering the compatibility of carbon electrodes and electrolytes, the electrochemical performance of EDLCs is evaluated not only based on the exposed surface area of the carbon electrodes, but also on the optimization of the pore-size distribution of the carbon. Certain studies have reported that micropores in carbon materials that feature pore sizes close to that of electrolyte ions or solvent-free IL ions create the maximal double-layer capacitance in charge storage.[27–33] Although the use of micropores leads to high capacitance values, the micropores restrict the migration of electrolyte ions and thereby give rise to a low power rating, especially in systems containing large electrolyte ions such as ILs. Using mesoporous carbons facilitates ion transportation, but this may adversely affect volumetric capacitance and thus limit the practical uses of the carbons.[34–39]

In this study, we investigated the formation of electric double layers of ILs in EDLCs at various voltages and charging rates. Carbons featuring various pore-size distributions were used to test two ILs of distinct sizes. We determined that whereas micropores are required for obtaining not only high capacitance values but also stable operation at high voltages, mesopores effectively assist ion transport into micropores across the entire voltage range. However, template mesoporous carbon (tMC) containing few micropores cannot accommodate ions at high voltages, which might induce IL-ion intercalation into graphitic edges. This study demonstrates, for the first time, the essential role of micropores in EDLCs assembled using ILs. Activated mesophase pitch (aMP) that features a hierarchical pore structure exhibits ultrahigh volumetric energy density in IL-based EDLCs.

2. Experimental

2.1. Materials

The carbon powders used for assembling EDLCs consisted of 95 wt% of porous carbon as the active material and 5 wt% of multi-walled carbon nanotubes (UniRegion Bio-Tech, UR-NTM005; 10–30 nm in outer diameter and 5–15 μm in length) as the conductive medium.[40,41] We used three types of porous carbons to assemble EDLCs: aMP, activated carbon fiber (aCF), and tMC.

The aMP carbon was prepared by heating mesophase pitch impregnated with KOH at a KOH/pitch ratio of 4.[42,43] The mesophase pitch used in this study was provided by China Steel Chemical Co., Taiwan. After mixing, the pitch–KOH slurry was vacuum-dried at 110 ℃ for 24 h. The dried sample was heated at 800 °C for 1 h in a horizontal cylindrical furnace purged using N_2. The KOH-etched product was washed sequentially with 0.5 M HCl solution and distilled water until the pH of the water–carbon mixture was >6. The aCF carbon was derived from milling a polyacrylonitrile-based activated carbon fiber cloth supplied by Challenge Carbon Technology Co., Taiwan.[44,45] The tMC carbon was obtained using a conventional silica-template method.[34–37] We also used non-porous graphite sheets (Merck, >99.99%) to compare with the porous carbons in electrochemical measurements.

Prior to any characterizations and electrochemical measurements, the carbons were heated in an Argon atmosphere at 900 °C for 20 min to remove surface oxides that are known to substantially reduce the electronic conductivity of carbon electrodes.[46]

The ILs used were 1-ethyl-3-methylimidazolium

bis(trifluoromethylsulfonyl)imide (EMIm-TFSI) and 1-methyl-1-propylpyrrolidinium bis(trifluoromethylsulfonyl)imide (MPPy-TFSI), which were supplied by Tokyo Chemical Industry Co., Japan. The sizes (width × length) of the cations EMIm and MPPy and the anion TFSI were 0.43 × 0.76 nm, 0.49 × 0.78 nm, and 0.29 × 0.79 nm, respectively (see Fig. S1 of the ESI†).[19–26]

2.2. Measurements

The specific surface area and porosity data were assessed by performing N_2 adsorption-desorption at 77 K by using an adsorption apparatus (Micromeritics, ASAP 2020, USA). The N_2 sorption was conducted at relative pressures (p/p_0) of 10^{-5}–1. The samples were heated at 400 °C for 12 h before analyzing sorption. We used the Brunauer–Emmett–Teller (BET) method to obtain the apparent surface area of the porous carbons, the density functional theory (DFT) to determine realistic surface areas and pore volumes, and the Barrett–Joyner–Halenda (BJH) method to calculate the pore-size distribution of mesopores. We analyzed the effect of carbon graphitic-layer intercalation on charge storage by measuring X-ray diffraction (XRD) by using a diffractometer (Rigaku, Ultima IV, Japan) featuring Cu Kα radiation, excited at 40 kV and 40 mA.

The electrochemical performance of EDLC cells was analyzed using a symmetrical two-electrode capacitor configuration. To prepare the electrodes, 2 mg of carbon powder was coated on titanium foils (1 cm^2 active area) and fixed under pressure without using a binder. The symmetrical cell consisted of two carbon electrodes that faced each other and sandwiched a cellulose filter paper (roughly 30 μm thick) as the separator. Electrochemical properties were measured at room temperature (approximately 25 °C) under an Argon atmosphere by using the ILs

EMIm-TFSI and MPPy-TFSI as the electrolytes. Cyclic voltammetric characterization of the EDLC cells was conducted within the stable voltage window at varying scan rates, using an electrochemical analyzer (Solartron Analytical, Model 1470E, UK). An AC electrochemical impedance spectroscopy (EIS) analyzer (Zahner-Elektrik IM6e, Germany) was used to measure the impedance behavior of capacitor cells at zero-, intermediate-, and high-voltage biases at an AC voltage amplitude of 5 mV and a frequency range of 5 mHz–200 kHz. The performance of EDLC cells was recorded using the electrochemical analyzer by measuring the galvanostatic charge–discharge values of the symmetric cells.

3. Results and Discussion

3.1. Characterization of the Electrode Materials

Fig. 1 presents the N_2-sorption isotherms of aMP, aCF, and tMC at 77 K. The aMP isotherm (Fig. 1a) shows strong adsorption at low relative pressures, indicating that micropores contributed greatly to the porosity of the aMP carbon. The broad-knee feature reflects the wide size distribution of the micropores. The aMP carbon also contained mesopores, which resulted in sorption hysteresis at high pressures. The isotherm of aCF (Fig. 1b) exhibits a sharp rise in the adsorbed volume at low pressures and a nearly horizontal plateau at high pressures, indicating the microporous nature of aCF. The isotherm of tMC (Fig. 1c) exhibits dominant adsorption at $p/p_0 > 0.4$ and marked hysteresis, indicating that tMC is mostly mesoporous. The pore volumes and surface areas of the carbons calculated based on the isotherms are summarized in Table 1. The BET surface area (S_{BET}) of aMP was calculated to be

3100 m^2g^{-1}, which is unrealistic because the BET method is not suitable for micropore analysis. We also used DFT to determine the total surface area (S_t) and pore volume (V_t). The S_t values measured for aMP, aCF, and tMC were 1920, 840, and 880 m^2g^{-2}, respectively, whereas tMC had the greatest V_t value (Table 1).

Fig. 2 shows the pore-size distribution of carbon mesopores determined by the BJH method. The shape of pore-size distributions revealed that tMC contained mainly mesopores, whereas micropores contributed substantially to the pore volumes of aMP and aCF. Mesopores provide passages for ion transport into micropores and are therefore essential for high-power operations.[36–39,47] Micropores, which feature sizes close to that of electrolyte ions, contribute considerably to surface area and thereby to double-layer formation. Table 1 lists the micropore surface area (S_{mi}) and the proportions of micro- and mesopores determined from DFT. The micropores made minor contributions to the total surface area and pore volume for tMC, in agreement with the BJH analysis. Although aCF had a higher proportion of micropores, aMP had a greater micropore volume than aCF because aMP was more porous by comparison.

3.2. Electrochemical Analysis of the Carbons

In this study, we used symmetric two-electrode cells to analyze the electrochemical performance of the carbons. Each carbon film contained carbon nanotubes (5 wt%) that connected the carbon particles (95 wt%) to improve electronic conductivity. Each electrode consisted of a 2-mg carbon film coated on a titanium foil featuring an active area of 1 cm^2. Fig. 3a presents the cyclic voltammograms of cells assembled using different carbons soaked in the EMIm-TFSI IL. The voltammograms obtained by scanning the cells within 0–3.5 V at 50 mV s^{-1} were rectangular, which is typical of an ideal capacitor. By comparison, the voltammograms assembled using the

MPPy-TFSI IL (Fig. 3b) exhibited a wider voltage window (4.1 V), but these were also rectangular. Because MPPy-TFSI features a larger cation size and is more viscous than EMIm-TFSI,[19–26] low currents were obtained in the cyclic scans of the aMP and aCF carbons that contain a larger amount of micropores. By contrast, the mesoporous tMC showed a greater current with MPPy-TFSI relative to that with EMIm-TFSI, mainly resulting from the formation of bumps in both scan directions. The bumps may be associated with strong interaction between the ionic molecules and the carbon surface.

Fig. 4a presents the cyclic voltammograms that were generated for the tMC cell assembled using MPPy-TFSI when the voltage widow was extended gradually from 2.0 to 4.1 V. The voltammograms showed typical capacitive behaviors at narrow voltage windows, and the bumps became evident when the voltage window was increased to 3 V or above. When the direction of voltage-window variation was reversed, the bumps created at high voltages retained their appearance even in the narrow-window scans (Fig. 4b). The scans performed at high voltages might have intercalated ions into the graphitic layers on the pore walls of tMC and created tunnels that store charge, with ion insertion into and retreat from the small tunnels accounting for the bumps appearing in the cyclic voltammograms. We also analyzed the aMP cell similarly as we analyzed tMC (see Fig. S2 of the ESI†) and determined that the aMP cell did not show intercalation bumps when the voltage window was widened. The structure of aMP might suppress the ion-intercalating mechanism that occurs at high voltages.

We verified the occurrence of graphitic-layer intercalation by using a symmetric cell consisting of two graphite-sheet electrodes and the MPPy-TFSI electrolyte. Graphite sheets exhibit sharp crystalline peaks in XRD analysis whereas the graphitic

crystal domains of porous carbons are too small to be analyzed by XRD. Fig. 5 (a and b) presents the XRD peaks of the as-received graphite-sheet and the graphite electrodes treated with cyclic scanning within different voltage ranges at 50 mV s^{-1} for 200 cycles. The as-received graphite exhibited a strong (002) peak at $2\theta = 26.3°$. After the cyclic scanning, both the positive and negative electrodes of the scanned cell exhibited (002) peaks of substantially lower intensities than those generated before the scans. Enlarging the voltage scan range weakened the diffraction peak intensity. The focused patterns observed in Fig. 5 (c and d) reveal that the voltage scan widened the (002) peak of graphite, indicating that intercalation occurred and reduced the size of the graphitic domains. The positive electrode scanned to 4 V exhibited an additional peak at 24.7°, which might result from intercalation of the relatively small TFSI anion. This crystal analysis confirmed the possibility of ions being intercalated into the graphitic layers of EDLC carbon electrodes.

We further analyzed the cells by using EIS, which distinguishes the capacitance and resistance values in the charge-storage process. Figs. 6 and 7 present the Nyquist spectra in the impedance-complex plane measured for cells assembled using EMIm-TFSI and MPPy-TFSI electrolytes, respectively. Panels (a), (b), and (c) of the figures show the results of impedance analyses applied with zero-, intermediate-, and high-voltage biases, respectively. In the inset in Fig. 6a, selective magnification is used to show the typical shapes of the impedance spectra in the high-frequency region. All the high-frequency spectra obtained at various voltages showed a transitional Warburg region, which was followed by a transformation into a vertical line with decreasing frequency. The intercept at the real axis of the impedance spectra corresponds to the equivalent-series resistance (R_{es}) of the cells. Extrapolating the low-frequency vertical line to intersect the real impedance axis yields the sum of R_{es}

and the Warburg resistance (R_W). The R_W values were obtained by subtracting the R_{es} from the intercept value. Fig. S3 of the ESI† presents a summary of the R_{es} and R_W values obtained at distinct bias voltages. The cells assembled using MPPy-TFSI exhibited larger R_{es} and R_W values than did the cells containing EMIm-TFSI because compared with EMIm-TFSI, MPPy-TFSI is more viscous and has a larger cation size.[14,48]

The R_{es} values, which feature the electric-field-driven drift motion of ions, were similar for the distinct carbons at zero and intermediate voltages. Bias at the highest voltage increased the R_{es} value substantially because of intensified ion penetration into micropores.[49] The aMP carbon had the largest micropore volume and therefore exhibited the largest R_{es} at the highest voltage bias. The R_W values are associated with ion diffusion in the pores. Thus, tMC, which has the largest pore size, exhibited the smallest R_W values, whereas aMP had the largest R_W values because its high microporosity severely restricted ion diffusion. The high-frequency impedance data indicate that mesopores assisted ion transport and that the resistance increased with an increase in the micropore depth accessed by ions. A high-voltage bias helped ions access micropores but enhanced transport resistance, particularly the resistance associated with drift motion.

In terms of the low-frequency zones regarding charge storage, all the cells exhibited vertical lines at 0 V in the full-range spectra (Figs. 6 and 7), indicating robust capacitive behaviors of these carbon-IL systems. Inclination away from the vertical position in the low-frequency spectra indicates the presence of restricted ion transport or chemical reaction in the double-layer charge-storage process.[49–53] In the EMIm-TFSI system, the extent of inclination of the low-frequency straight lines increased with decreasing pore size of the carbons biased at 0 V (i.e., aCF > aMP >

tMC in the inclination extent) (Fig. 6a), demonstrating that pore diffusion governs the charge-storage mechanism under low-voltage bias conditions. When the voltage bias was increased (Fig. 6, panels b and c), the extent of inclination measured for all the carbons increased. This result indicates that the pores involved in charge storage at high voltage biases are deeper or smaller than those involved at low voltage biases, and that the area accessible for charge storage varies with the applied voltage. Under a 1.75-V bias, the inclination extent displayed an order of aMP > aCF > tMC, indicating that the deep micropores in aMP caused a high pore-diffusion resistance (Fig. 6b). When the bias was increased to 3.5 V, the inclination extent of the low frequency lines in the spectra showed an order of tMC > aCF > aMP (Fig. 6c). Because tMC lacked the micropores that accommodate ions at high voltages, charge storage by means of the intercalation of ions into graphitic layers might have caused such a marked deviation from optimal capacitive behavior. The bumps in the wide-range cyclic voltammograms of the tMC cell (Fig. 4) have suggested the occurrence of graphitic-layer intercalation in the micropore-deficient tMC carbon.

Similar to the EIS results of the EMIm-TFSI system, the EIS results obtained for MPPy-TFSI revealed that increasing the bias voltage enhanced the spectrum-line inclination because of increased transport resistance in the small or deep pores of this IL (Fig. 7). Compared with using EMIm-TFSI, the use of MPPy-TFSI resulted in greater inclination because of this IL's larger cation size. The carbons were similarly affected by bias voltage in the charge-storage process when the two electrolytes were used: tMC exhibited the lowest resistance at low and intermediate voltages (observed as the least inclination of the low-frequency spectra), whereas aMP displayed a less restricted charge storage at the highest voltage. Because aMP contains the largest amount of micropores, the results in Figs. 6 and 7 indicate that the presence of

micropores was indispensable for double-layer charge storage at high voltages.

To verify that micropores are indispensable for high-voltage operation, we subjected the non-porous graphite sheets to impedance analysis and compared the results with those of the porous carbons (Figs. 6 and 7). The low-frequency lines of the graphite electrode were considerably more inclined than those of the porous electrodes at all bias voltages. Even at zero- and intermediate-voltage biases, the non-porous graphite electrode exhibited lines that were substantially inclined, indicating that the porous structure is essential for double-layer charge storage.

The results in Figs. 6 and 7 explicitly revealed that the surface of the porous carbons was not evenly used at distinct voltages and that inner or small pores were accessible only at high voltages. The tMC electrode contained few micropores to allow IL-ion penetration at high voltages. Under such a circumstance, the IL ions would likely be intercalated into the exposed prismatic domains of the pore wall to create high-voltage capacitance (Scheme 1a). The aMP and aCF carbons that contain micropores exhibited a less restricted charge-storage process at high voltages than did tMC carbon. The aMP carbon in particular, which featured a hierarchical pore structure consisting of adequate proportions of mesopores and micropores, exhibited remarkably smaller resistance for ion motion at high voltages than did the other carbons (Scheme 1b). The small micropores may have accommodated single IL ions that dissociated from their counter ions before entering the micropores. This micropore-penetrating mechanism may contribute to the majority of the double-layer capacitance at high voltages.

To present the capacitive response clearly, we converted the impedance-complex planes shown in Figs. 6 and 7 into capacitance-complex planes (Fig. 8), which show the real and imaginary components of the capacitance, Re(C) and Im(C), respectively,

as a function of modulation frequency (f).[49,54,55] The following formula provides such a capacitance:

$$\mathrm{Re}(C) + j\mathrm{Im}(C) = \frac{1}{j\omega Z} = \frac{1}{j\omega[\mathrm{Re}(Z) + j\mathrm{Im}(Z)]} \qquad (1)$$

where j is the imaginary unit ($j = \sqrt{-1}$), ω is the angular frequency and is equal to $2\pi f$, and Z is the overall impedance of the capacitor cells. A uniform charge-storage pattern in AC analysis is characterized by a single semicircle feature in the complex plane. Fig. 8 (panels a, b, d, and e) shows single-semicircle characteristics in the capacitance-complex planes determined for the cells applied with zero and intermediate voltages; these characteristics indicate that charge storage occurs uniformly in response to double-layer formation at the electrode-electrolyte interface. In high-voltage operations, the semicircles in the complex plane transformed into straight-line resistive tails at low frequencies (Fig. 8, panels c and f).[52] The transformation reflects a marked increase in resistance, which likely results from ions being intercalated into the graphitic layers. Among the three carbons, tMC displayed the highest capacitance contribution from the intercalation mechanism, which was reflected by the low-frequency straight lines. The capacitance spectra of the micropore-rich aMP and aCF carbons exhibited a more intact semicircle feature than did tMC, indicating that the regular double-layer charge storage on the carbon surface created most of the capacitance. The large S_{mi} or micropore volume of the aMP carbon (Table 1) effectively suppressed the intercalation process.

Fig. 9 (a and b) shows the voltage-time curves of the cells observed with a galvanostatic charge–discharge at 10 A g^{-1} in the two IL electrolytes. All the cells exhibited a standard capacitive behavior under the widest voltage windows allowable for the electrolytes. The IR drop of the cells, which is a sudden voltage drop at the

onset of the galvanostatic discharge, shows an order of aMP > aCF > tMC, agreeing with the high-frequency EIS analysis. The tMC carbon, which contains a high proportion of mesopores, helped reduce the series resistance of the cells. Fig. 9 (c and d) shows the variation of Coulombic efficiency in relation to the galvanostatic charge–discharge cycle. The aMP and aCF carbons, which contain numerous micropores that can accommodate IL ions, exhibited Coulombic efficiencies close to 100%. Conversely, in the case of tMC, the intercalation of ions into the graphitic layers might have resulted in chemical reaction between the ions and the graphitic sheets and led to lower Coulombic efficiency relative to those of aMP and aCF.

3.3. Capacitive Performance of the Resulting EDLCs

We used the galvanostatic charge–discharge operation (Fig. 9) to calculate the capacitance values. The specific electrode capacitance (C_m) were calculated according to: $C_m = 4\times I\times t_d/(M\times\Delta V)$, where I is the discharge current, t_d the discharge time, M the total carbon mass of two symmetric electrodes, and ΔV the voltage difference in discharge excluding the IR drop. Fig. 10 presents the C_m values of the carbon electrodes discharged at various currents. Because of their lower ion-transport resistance, the cells assembled using EMIm-TFSI (Fig. 10a) showed higher capacitance retention at high discharge rates than did the cells assembled using MPPy-TFSI (Fig. 10b). Examining the effect of carbon type revealed that the aCF cells poorly retained capacitance at high discharge rates because aCF lacked the mesopores that facilitate ion transport; because of the presence of mesopores, the aMP and tMC cells retained considerably more capacitance than did the aCF cells. The aMP cells were superior to the tMC cells primarily because the micropores of the aMP carbon accommodated ions at high bias voltages and thereby lowered charge-storage

resistance (Figs. 6c and 7c).

The aMP and tMC cells were charged and discharged in EMIm-TFSI (0–3.5 V) and MPPy-TFSI (0–4.1 V) at 10 A g^{-1} for 10000 cycles to confirm the the stability of capacitance with cycling. The aMP cells exhibited high cycling stability even at such high operating voltages (see Fig. S4 of the ESI†), showing a capacitance retention of 90% after 10000 cycles. The minor capacitance decay may result from gradual carbon structure change caused by the IL-ion attack at high voltages. The tMC cells were less stable in the cycling test by showing approximately 80% capacitance retention. The above cycle-life comparison demonstrates again the importance of micropores in aMP for high-voltage operations.

According to the galvanostatic discharge data, Fig. 11 shows a summary of the power and energy densities of the aMP and tMC symmetric cells based on the mass and volume of the carbon electrodes. The gravimetric power (P_{cell}) and energy (E_{cell}) are obtained with $P_{cell} = I \times \Delta V / (2M)$ and $E_{cell} = P_{cell} \times t_d$. All the cells have high gravimetric energy and power values because of the highly accessible porosities of aMP and tMC and the wide voltage range of the electrolytes. Using MPPy-TFSI for wide voltage range operation, Fig. 11a shows that the aMP cell reached a high gravimetric energy value of 105 Wh kg^{-1} and sustain 50 Wh kg^{-1} at a high power of 50 kW kg^{-1}. The tMC cell exhibited similar performance because the large pores of tMC facilitated the transport of the large MPPy ions. The aMP cell assembled with the EMIm-TFSI electrolyte reached a gravimetric energy of only 78 Wh kg^{-1} with an operating voltage of 3.5 V, whereas this cell exhibited a superior power of 57 kW kg^{-1} for delivering an energy of 50 Wh kg^{-1}. Using EMIm-TFSI as the electrolyte, the performance of the tMC cell (based on the specific power and energy values, Fig. 11a) was evidently inferior to that of the aMP cell because tMC lost the large-pore

advantage when small ions were used.

In terms of volumetric power and energy, Fig. 11b shows that the aMP cells substantially outperformed the tMC cells in both electrolyte systems owing to the compact structure of aMP, which had a high bulk density of 0.50 g cm^{-3}. The density of tMC was only 0.30 g cm^{-3} because of the mesoporous feature of tMC. The aMP cell reached a high volumetric energy of 50 Wh L^{-1} with MPPy-TFSI and a high power of 43 kW L^{-1} with EMIm-TFSI.

We also calculated the stack volumetric power and energy of the 1-cm^2 aMP EDLCs on the basis of the total volume of all capacitor elements including the current collectors (50 μm thick each), separator (30 μm thick), and carbon electrodes (40 μm thick each), but no packaging materials. Fig. 12 shows the comparison of the stack volumetric power and energy of the aMP EDLCs with those of other capacitors reported in literature and commercially-available electrochemical devices.[16,56–60] The aMP|EMIm-TFSI EDLC (3.5 V/90 mF) reached a stack energy of 14 mWh cm^{-3} and a power of 17 W cm^{-3}; aMP|MPPy-TFSI EDLC (4.1 V/85 mF) delivered 19 mWh cm^{-3} and 12 W cm^{-3}. These data of these aMP EDLCs represent the state-of-the-art performance for conventional sandwich-type EDLCs, particularly the stack energy being more than an order of magnitude higher than those of the commercial-product and previous studies.[56] Electrolytic capacitors and some planar micro-EDLCs exhibited power rates higher than those of the aMP EDLCs, but their energy values were lower.[16,57–60] The ultrahigh stack volumetric energy of the aMP EDLCs demonstrates the critical role of a hierarchical pore structure (Scheme 1b), consisting of both micropores and mesopores, in high-voltage EDLC operation.

4. Summary and Conclusions

This study has demonstrated that micropores are indispensable for high-voltage EDLCs assembled using ILs. Micropore-rich aMP and aCF carbons exhibited lower resistance in high-voltage charge storage than did the micropore-deficient tMC carbon. Micropores can accommodate single ions dissociated from their counter ions at high voltages. Ions were intercalated into the graphitic layers on the pore walls at high voltages when the carbon contained no or few micropores. The intercalation not only led to high charge-storage resistance, but also caused chemical interaction between ions and graphitic layers. However, mesopores facilitated ion transport by means of drift and diffusion processes and suppressed the charge-storage resistance at low and intermediate voltages. The aMP carbon, which featured a hierarchical pore structure consisting of suitable proportions of micropores and mesopores, retained capacitance effectively under high-rate and wide-voltage charge–discharge operations. The compact framework comprising packed turbostratic graphene sheets makes aMP superior to other high porosity carbons for volumetric energy and power densities.

Acknowledgements

This research was supported by the Ministry of Science and Technology, Taiwan (101-2221-E-006-243-MY3, 101-2221-E-006-225-MY3, 103-3113-E-006 -009, and 102-3113-E-006-002), and by the Ministry of Education, Taiwan, The Aim for the Top University Project to the National Cheng Kung University.

† **Electronic Supplementary Information (ESI) available**: Chemical structures of

EMIm-TFSI and MPPy- TFSI; cyclic voltammograms of the aMP cell obtained by varying the voltage window in MPPy-TFSI; variation of the R_{es} and R_W with the applied voltages for different cells; capacitance retention with cycle number for the aMP and tMC symmetric cells. See DOI: 10.1039/b000000x/.

References

1. B. E. Conway, Electrochemical Supercapacitors: Scientific Fundamentals and Technological Applications, Plenum Publishers, New York, **1999**.
2. R. Kötz and M. Carlen, *Electrochimica Acta* 2000, **45**, 2483–2498.
3. A. Burke, *J. Power Sources* 2000, **91**, 37–50.
4. P. Simon and Y. Gogotsi, *Nature Materials* 2008, **7**, 845–854.
5. P. J. Hall, M. Mirzaeian, S. I. Fletcher, F. B. Sillars, A. J. R. Rennie, G. O. Shitta-Bey, G. Wilson, A. Cruden and R. Carter, *Energy Environ. Sci.* 2010, **3**, 1238–1251.
6. M. Ishikawa, M. Morita, M. Ihara and Y. Matsuda, *J. Electrochem. Soc*. 1994, **141**, 1730–1734.
7. Y. Matsuda, M. Morita, M. Ishikawa and M. Ihara, *J. Electrochem. Soc*.1993, **140**, L109– L110.
8. X. Yang, Y. S. He, G. Jiang, X. Z. Liao and Z. F. Ma, *Electrochemistry Communication* 2011, **13**, 1166–1169.
9. K. Fic, G. Lota, M. Meller and E. Frackowiak, *Energy Environ. Sci.* 2012, **5**, 5842–5850.
10. M. D. Stoller, S. Park, Y. Zhu, J. An and R. S. Ruoff, *Nano Lett.* 2008, **8**, 3498–3502.
11. P. Kurzweil and M. Chwistek, *J. Power Sources* 2008, **176**, 555–567.
12. A. B. McEwen, H. L. Ngo, K. LeCompte and J. L. Goldman, *J. Electrochem. Soc*. 1999, **146**, 1687–1695.
13. M. Galiński, A. Lewandowski and I. Stępniak, *Electrochimica Acta* 2006, **51**, 5567–5580.

14. F. B. Sillars, S. Isobel Fletcher, M. Mirzaeian and P. J. Hall, *Energy Environ*. *Sci*. 2011, **4**, 695–706.

15. T. Y. Kim, H. W. Lee, M. Stoller, D. R. Dreyer, C. W. Bielawski, R. S. Ruoff and K. S. Suh, *ACS Nano* 2011, **5**, 436–442.

16. M. F. El-Kady, V. Strong, S. Dubin and R. B. Kaner, *Science* 2012, **335**, 1326–1330.

17. H. Kurig, M. Vestli, K. Tõnurist, A. Jänes and E. Lust, *J. Electrochem*. *Soc*. 2012, **159**, A944–A951.

18. M. F. El-Kady and R. B. Kaner, *Nat*. *Commun*. 2013, *4:1475*, doi: 10.1038/ncomms2446.

19. K. R. Seddon, *J. Chem*. *Tech*. *Biotechnol*. 1997, **68**, 351–356.

20. S. Zhang, N. Sun, X. He, X. Lu and X. Zhang, *J. Phys*. *Chem*. *Ref*. *Data* 2006, **35**, 1475–1517.

21. J. Ranke, S. Stolte, R. Störmann. J. Arning and B. Jastorff, *Chem*. *Rev*. 2007, **107**, 2183–2206.

22. A. Balducci, R. Dugas, P. L. Taberna, P. Simon, D. Plée, M. Mastragostino and S. Passerini, *J. Power Sources* 2008, **185**, 1575–1579.

23. J. M. Wishart, *Energy Environ*. *Sci*. 2009, **2**, 956–961.

24. M. Armand, F. Endres, D. R. MacFarlane, H. Ohno and B. Scrosati, *Nature Materials* 2009, **8**, 621–629.

25. W. A. Henderson and S. Passerini, *Chem*. *Mater*. 2004, **16**, 2881–2885.

26. N. V. Plechkova and K. R. Seddon, *Chem*. *Soc*. *Rev*. 2008, **37**, 123–150.

27. E. Raymundo-Piñero, K. Kierzek, J. Machnikowski and F. Béguin, *Carbon* 2006, **44**, 2498–2507.

28. J. Chmiola, G. Yushin, Y. Gogotsi, C. Portet, P. Simon and P. L. Taberna, *Science* 2006, **313**, 1760–1763.

29. C. Largeot, C. Portet, J. Chmiola, P. L. Taberna, Y. Gogotsi, P. Simon, *J. Am. Chem. Soc.* 2008, **130**, 2730–2731.

30. J. Huang, B. G. Sumpter and V. Meunier, *Angew. Chem. Int. Ed.* 2008, **47**, 520–524.

31. J. Huang, B. G. Sumpter and V. Meunier, *Chem. Eur. J.* 2008, **14**, 6614–6626.

32. J. Chmiola, C. Largeot, P. L. Taberna, P. Simon and Y. Gogotsi, *Angew. Chem. Int. Ed.* 2008, **47**, 3392–3395.

33. D. Jiang, Z. Jin, D. Henderson and J. Wu, *J. Phys. Chem. Lett.* 2012, **3**, 1727–1731.

34. S. A. Al-Muhtaseb and J. A. Ritter, *Adv. Mater.* 2003, **15**, 101–114.

35. C. Vix-Guterl, E. Frackowiak, K. Jurewicz, M. Friebe, J. Parmentier and F. Béguin, *Carbon* 2005, **43**, 1293–1302.

36. W. Xing, S. Z. Qiao, R. G. Ding, F. Li, G. Q. Lu, Z. F. Yan and H. M. Cheng, *Carbon* **2006**, *44*, 216–224.

37. K. Xia, Q. Gao, J. Jiang and J. Hu, *Carbon* 2008, **46**, 1718–1726.

38. D. Saha, E. A. Payzant, A. S. Kumbhar and A. K. Naskar, *ACS Appl. Mater. Interfaces* 2013, **5**, 5868–5874.

39. Y. Mun, C. Jo, T. Hyeon, J. Lee, K. S. Ha, K. W. Jun, S. H. Lee, S. W. Hong, H. I. Lee, S. Yoon and J. Lee, *Carbon* 2013, **64**, 391–402.

40. D. Zhang, R. Cai, Y. Zhou, Z. Shao, X. Liao and Z. Ma, *Electrochim. Acta* 2010, **55**, 2653– 2661.

41. Y. Zhou, J. Wang, Y. Hu, R. O'Hayre and Z. Shao, *Chem. Commun.* 2010, **46**, 7151– 7153.

42. T. C. Weng and H. Teng, J. Electrochem. Soc. 2001, **148**, A368–A373.

43. M. F. Hsueh, C. W. Huang, C. A. Wu, P. L. Kuo and H. Teng, *J. Phys. Chem. C* 2013, **117**, 16751–16758.

44. H. Y. Liu, K. P. Wang and H. Teng, *Carbon* 2005, **43**, 559–566.

45. C. W. Huang, C. A. Wu, S. S. Hou, P. L. Kuo, C. T. Hsieh and H. Teng, *Adv. Funct. Mater*. 2012, **22**, 4677–4685.

46. Y. R. Nian and H. Teng, *J. Electrochem. Chem*. 2003, **540**, 119–127.

47. S. Yoon, J. Lee, T. Hyeon and S. M. Oh, *J. Electrochem. Soc*. 2000, **147**, 2507–2512.

48. F. B. Sillars, S. Isobel Fletcher, M. Mirzaeian and P. J. Hall, *Phys. Chem. Chem. Phys*. 2012, **14**, 6094–6100.

49. P. L. Taberna, P. Simon and J. F. Fauvarque, *J. Electrochem. Soc*. 2003, **150**, A292–A300.

50. P. Zoltowski, *J. Electrochem. Chem*. 1998, **443**, 149–154.

51. H. K. Song, H. Y. Hwang, K. H. Lee and L. H. Dao, *Electrochim. Acta* 2000, **45**, 2241–2257.

52. J. H. Jang, S. Yoon, B. H. Ka, Y. H. Jung and S. M. Oh, *J. Electrochem. Soc*. 2005, **152**, A1418–A1422.

53. D. Saha, Y. Li, Z. Bi, J. Chen, J. K. Keum, D. K. Hensley, H. A. Grappe, H. M. Meyer, S. Dai, M. P. Paranthaman and A. K. Naskar, *Langmuir* 2014, **30**, 900–910.

54. C. W. Huang, C. T. Hsieh, P. L. Kuo and H. Teng, *J. Mater. Chem*. 2012, **22**, 7314–7322.

55. H. C. Huang, C. W. Huang, C. T. Hsieh, P. L. Kuo, J. M. Ting and H. Teng, *J. Phys. Chem. C* 2011, **115**, 20689–20695.

56. M. D. Stoller and R. S. Rouff, *Energy Environ. Sci.* 2010, **3**, 1294–1301.

57. D. Pech, M. Brunet, H. Durou, P. Huang, V. Mochalin, Y. Gogotsi, P. Taberna and P. Simon, *Nature Nanotech*. 2010, **5**, 651–654.

58. F. Meng and Y. Ding, *Adv. Mater*. 2011, **23**, 4098–4102.

59. W. Gao, N. Singh, L. Song, Z. Liu, A. L. M. Reddy, L. Ci, R. Vajtal, Q. Zhang, B. Wei and M. Ajayan, *Nature Nanotech*. 2011, **6**, 496–500.

60. J. Lin, C. Zhang, Z. Yan, Y. Zhu, Z. Peng, R. H. Hauge, D. Natelson and J. M. Tour, *Nano Lett*. 2013, **13**, 72–78.

Table 1 Pore structure of the aMP, aCF, and tMC carbons. S_{BET} represents the surface area determined by the Brunauer–Emmett–Teller method, S_t and V_t the surface area and pore volume determined by the density functional theory, and S_{mi} the micropore (0.46–2 nm) surface area determined by the density functional theory.

Carbon	S_{BET} (m^2g^{-1})	S_t (m^2g^{-1})	S_{mi} (m^2g^{-1})	V_t (cm^3g^{-1})	Pore size distribution	
					Micro (%)	Meso (%)
aMP	3100	1920	1420	1.70	45	55
aCF	1180	840	740	0.60	57	43
tMC	1370	880	190	3.30	3	97

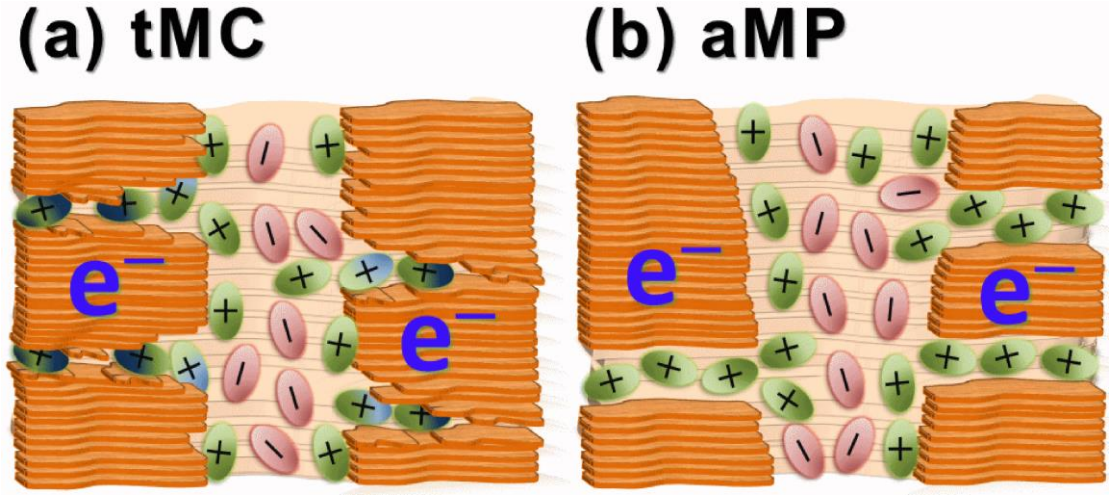

Scheme 1. Schematics showing the penetration behaviors of IL ions in two distinct carbons negatively charged at high voltages. (a) tMC; the IL ions would likely be intercalated into the exposed prismatic domains of the pore wall to create high-voltage capacitance. (b) aMP; the small micropores in aMP carbon may have accommodated single IL ions that dissociated from their counter ions before entering the micropores.

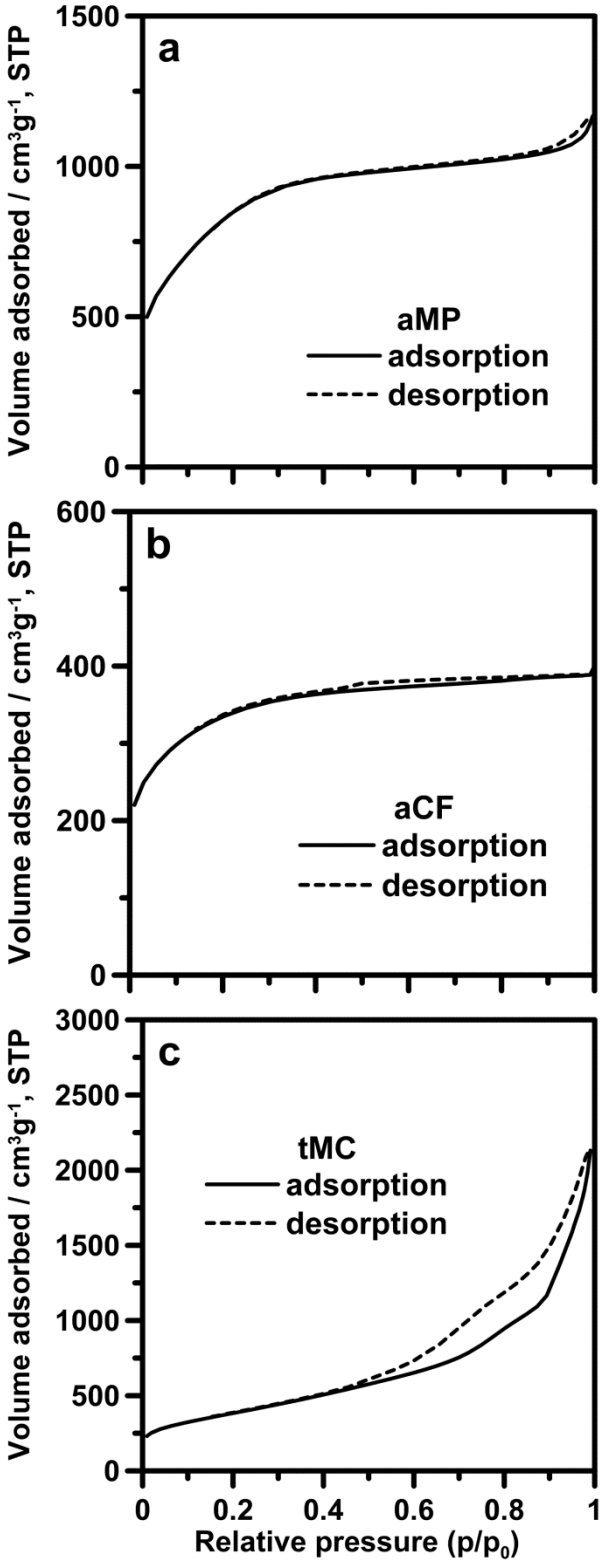

Fig. 1. N_2 adsorption (solid line)–desorption (dash line) isotherms of the porous carbons: (a) aMP, (b) aCF, and (c) tMC.

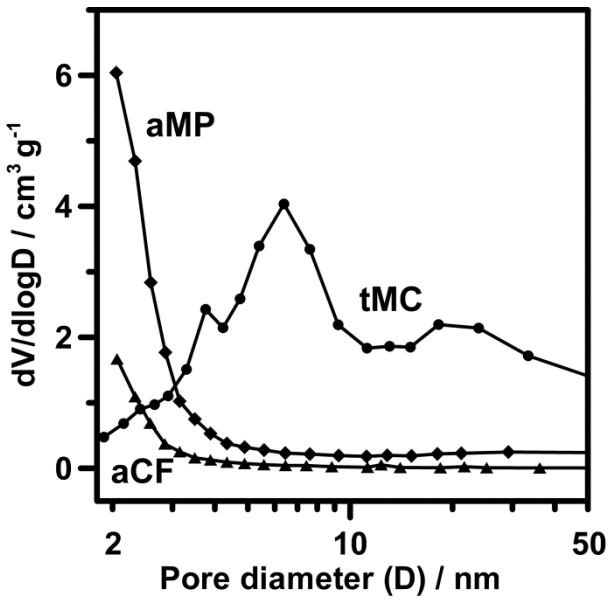

Fig. 2. Pore size distribution analysis based on the BJH method for the porous carbons.

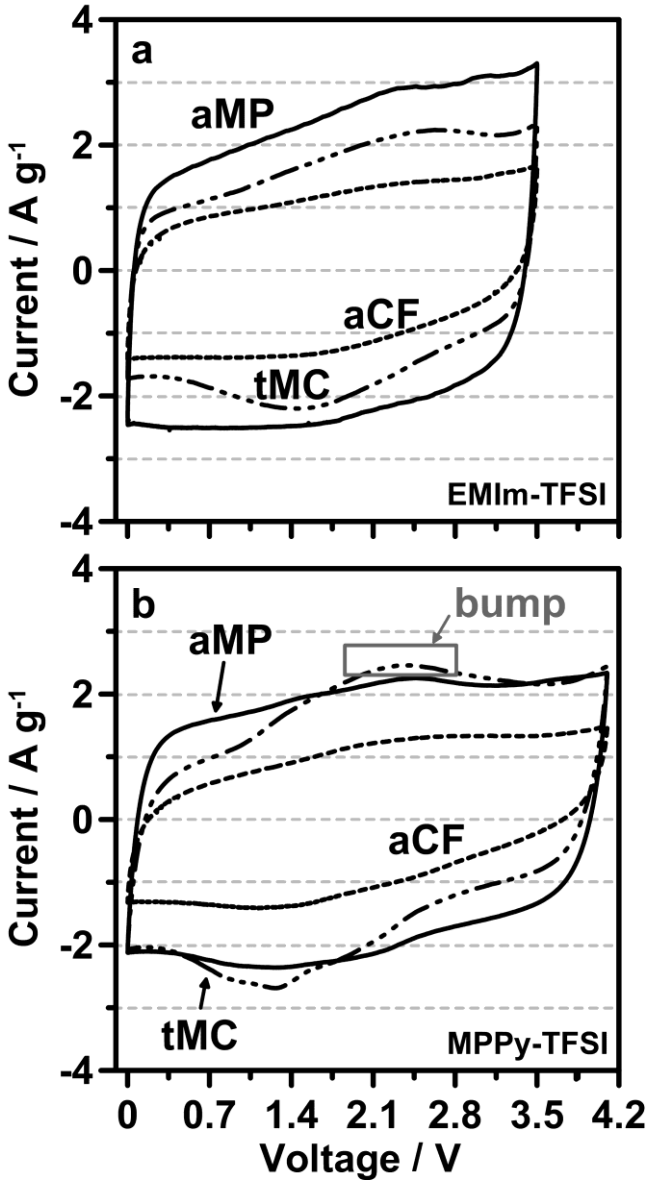

Fig. 3. Cyclic voltammograms of the symmetric aMP, aCF, and tMC two-electrode cells assembled with different ion-liquid electrolytes: (a) EMIm-TFSI; (b) MPPy-TFSI. The scans were performed with voltage windows of 3.5 and 4.1 V for EMIm-TFSI and MPPy-TFSI, respectively, at a scan rate of 50 mV s^{-1}.

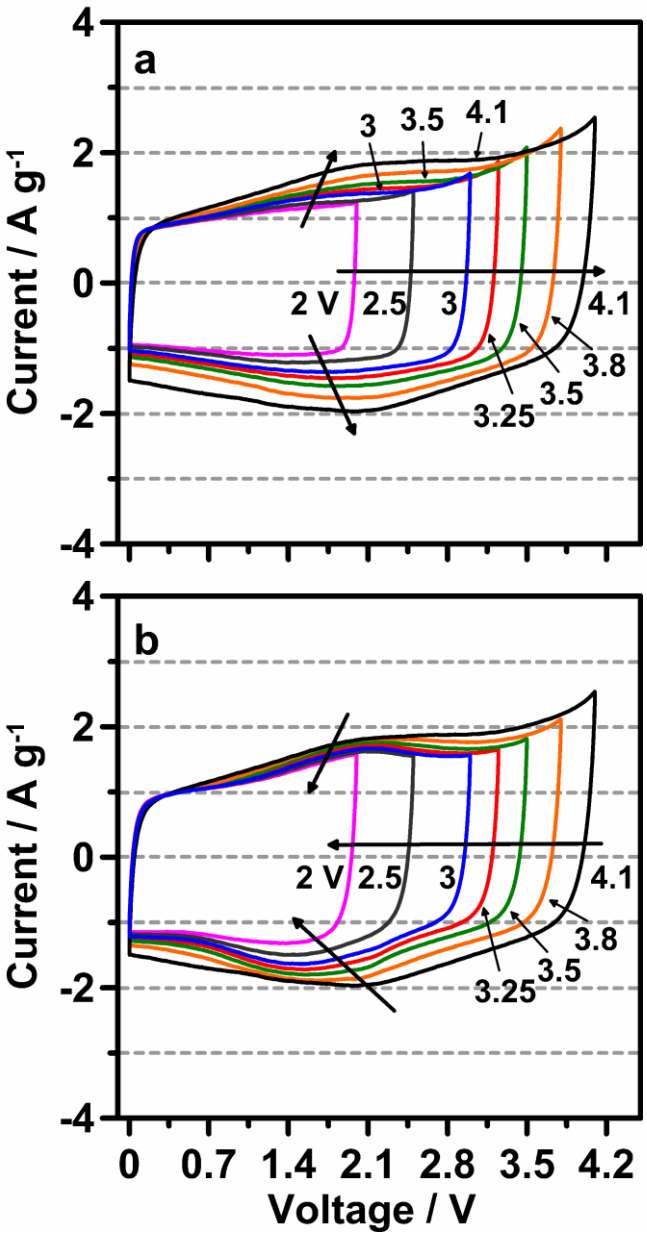

Fig. 4. Cyclic voltammograms of the symmetric tMC cell obtained sequentially by: (a) gradually extending the voltage window from 2 to 4.1 V; (b) reversing the direction of voltage-window variation from 4.1 to 2 V. The cell was assembled using MPPy-TFSI and operated at a scan rate of 50 mV s^{-1}.

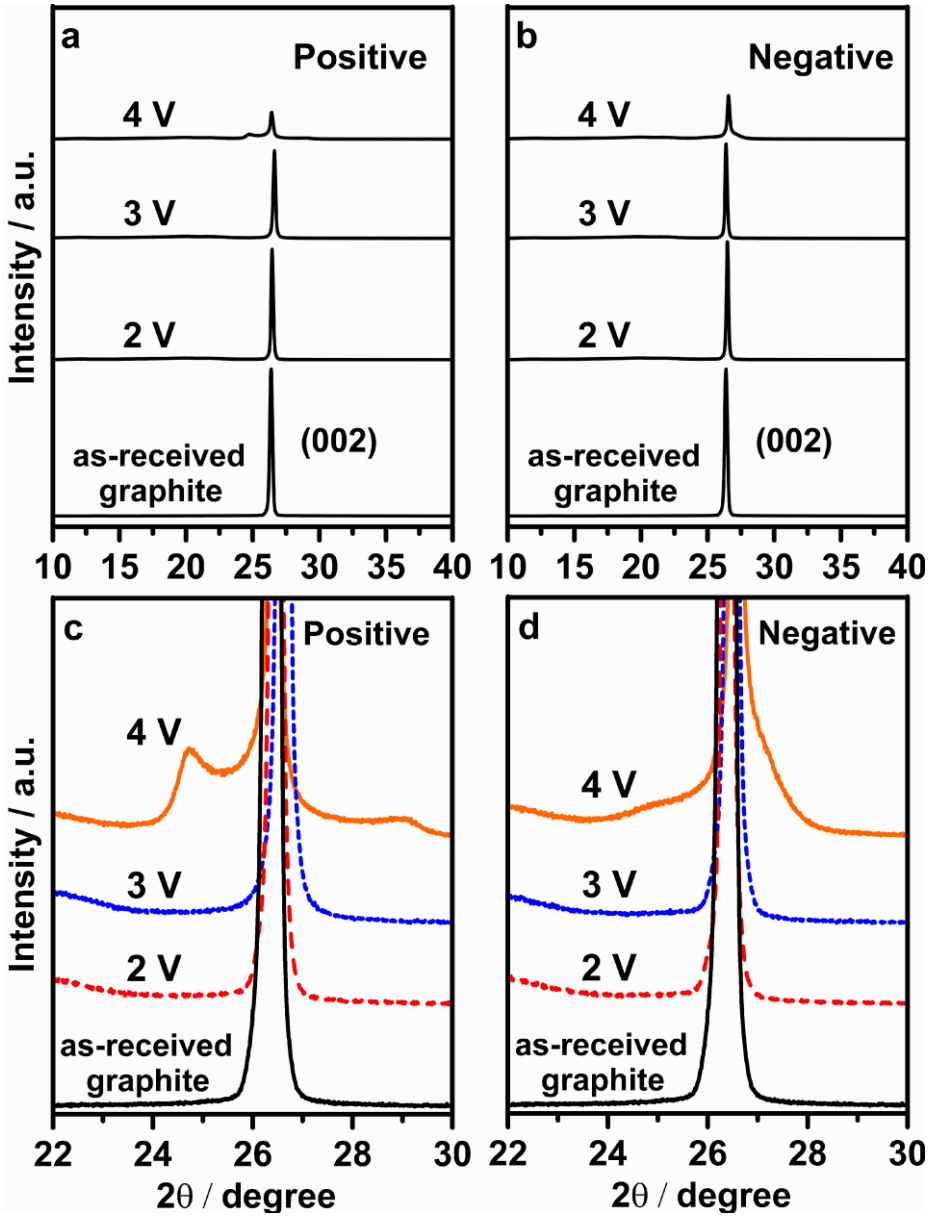

Fig. 5. (a,b) XRD patterns of the as-received graphite sheets and the positive and negative graphite sheets after cyclic scanning in MPPy-TFSI within different voltage ranges at 50 mV s^{-1} for 200 cycles. (c,d) The magnified (002) peaks of the graphite sheets shown in panels (a,b).

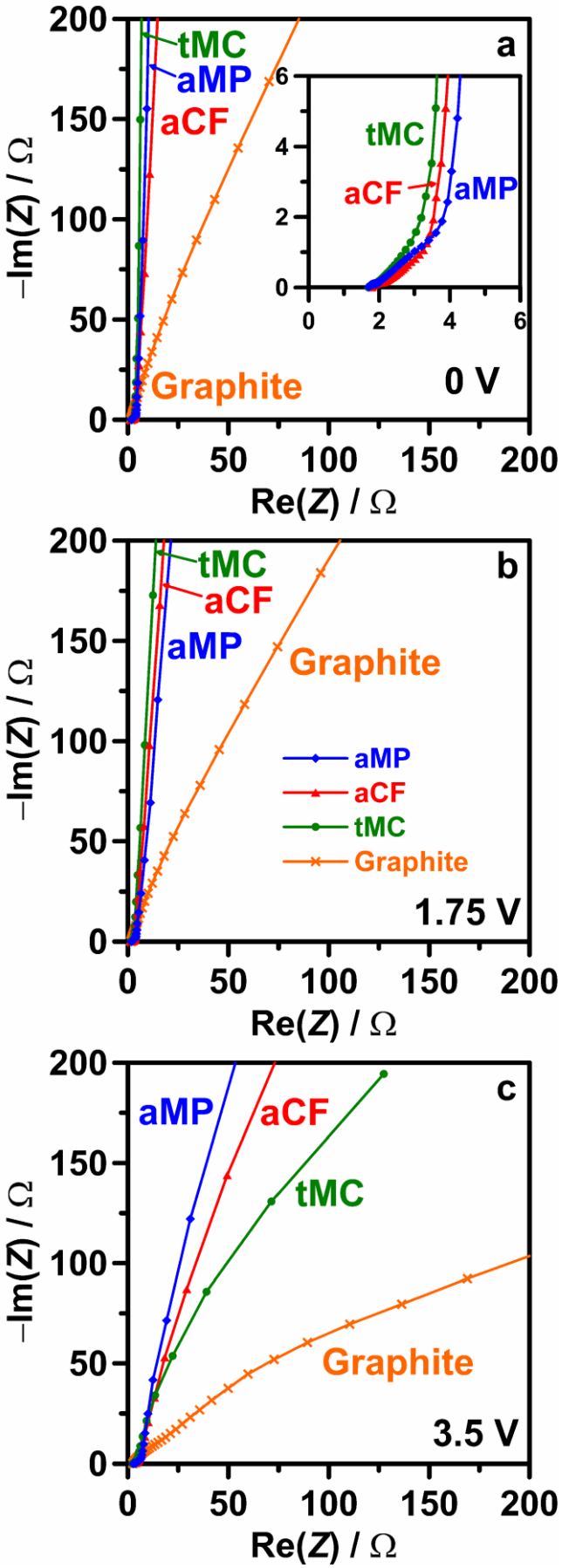

Fig. 6. AC Impedance complex-plane spectra of the aMP, aCF, tMC, and graphite

two-electrode cells assembled with EMIm-TFSI at varying voltage biases: (a) 0 V, (b) 1.75 V, and (c) 3.5 V. The inset of panel (a) shows a magnified view of the high frequency zone of the impedance spectra.

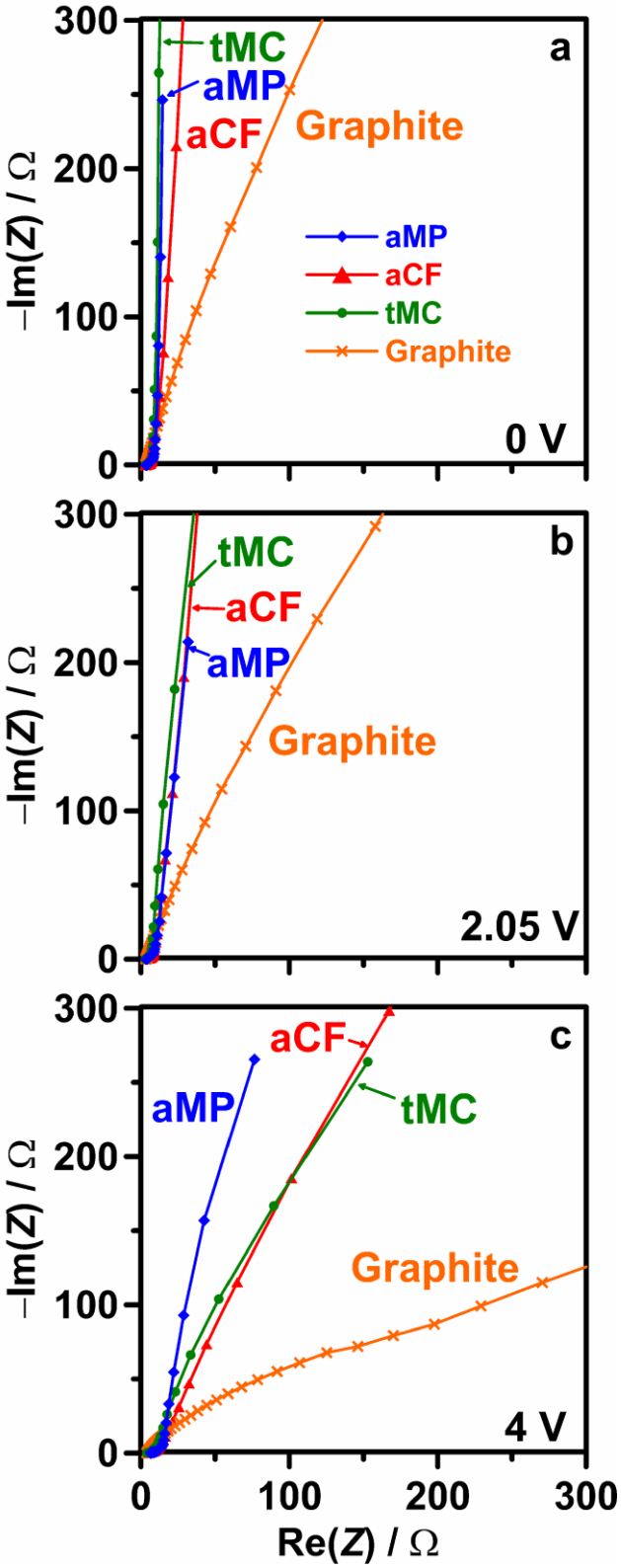

Fig. 7. AC Impedance complex-plane spectra of the aMP, aCF, tMC, and graphite two-electrode cells assembled with MPPy-TFSI at varying voltage biases: (a) 0 V, (b) 2.05 V, and (c) 4.0 V.

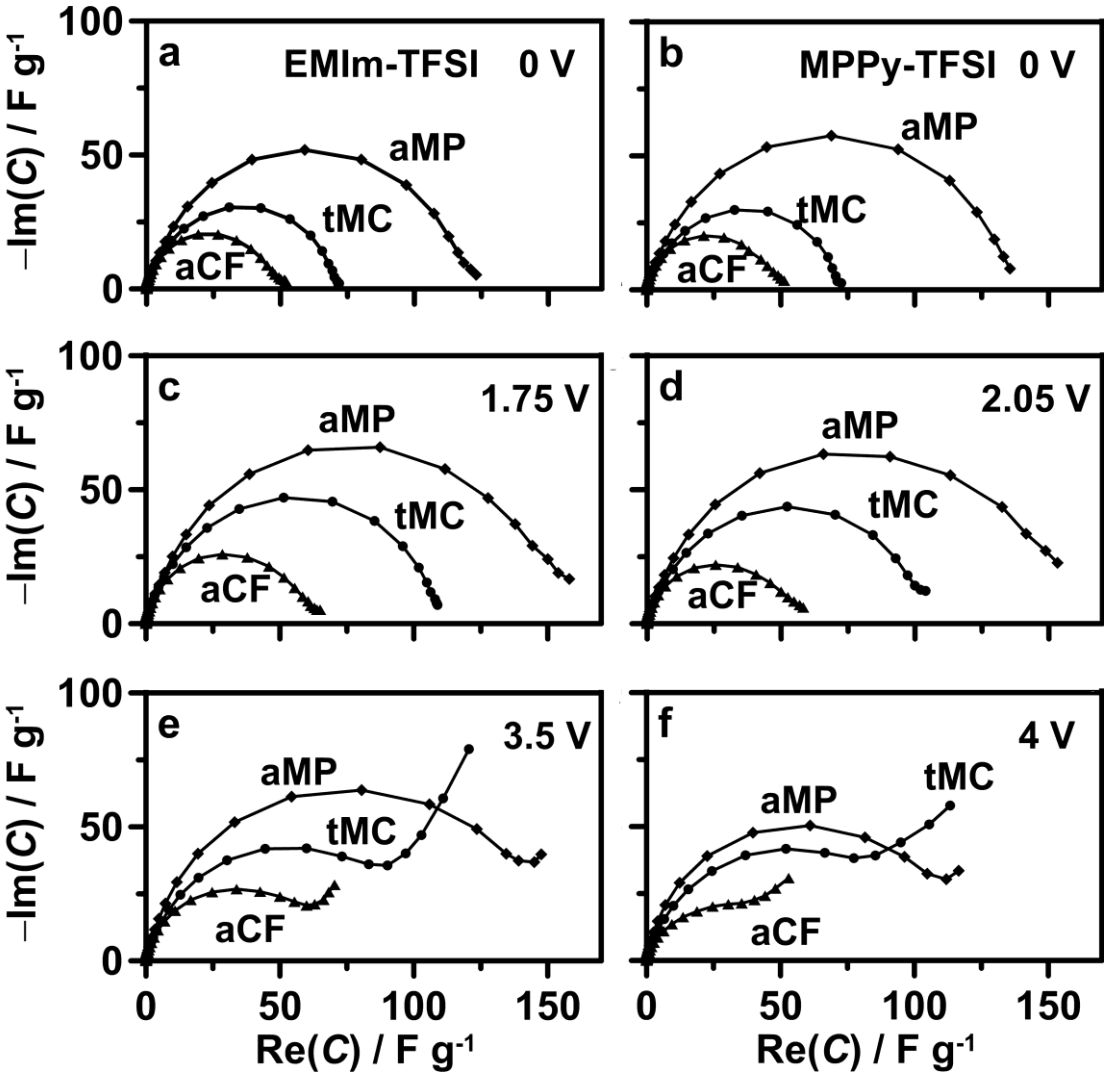

Fig. 8. Capacitance complex-plane spectra at varying voltage biases for the symmetric aMP, aCF, and tMC cells assembled with different electrolytes: (a,c,e) EMIm-TFSI; (b,d,f) MPPy-TFSI. The spectra were converted from the AC impedance spectra shown in Figs. 6 and 7 using Eq (1).

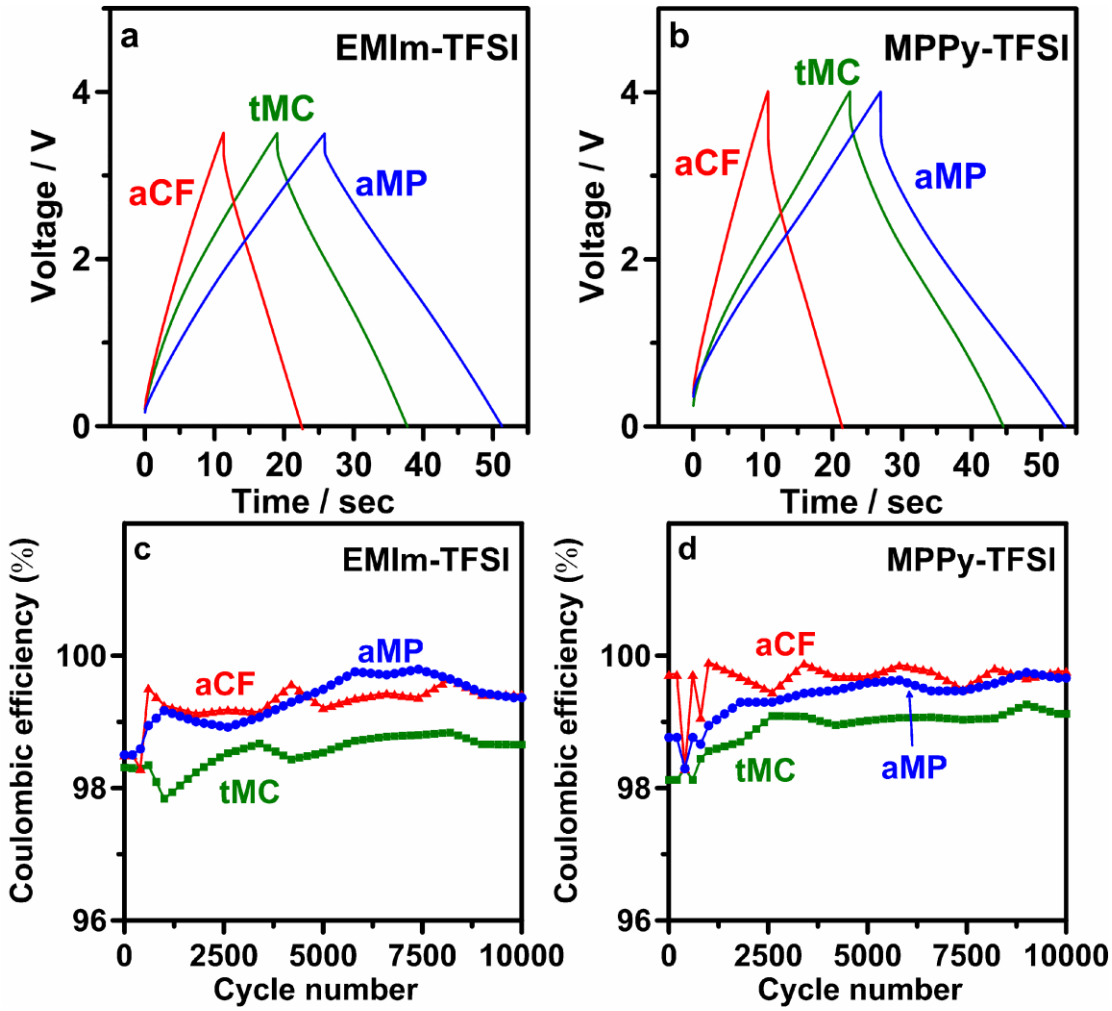

Fig. 9. (a,b) Typical voltage vs. time curves of the symmetric two-electrode aMP, aCF, and tMC cells assembled using EMIm-TFSI and MPPy-TFSI. (c,d) Variation of Coulombic efficiency with cycle number for the cells assembled using EMIm-TFSI and MPPy-TFSI. The data were obtained using galvanostatic charge–discharge at 10 A g^{-1} (40 mA cm^{-2}).

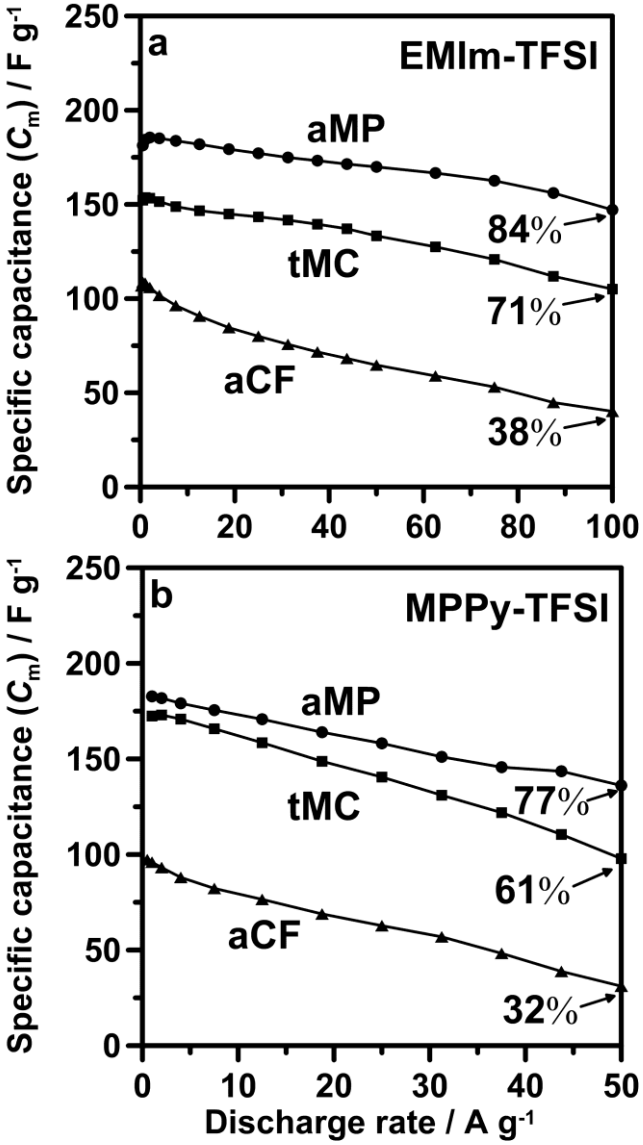

Fig. 10. Variation of specific capacitance with discharge rate for the symmetric two-electrode aMP, aCF, and tMC cells assembled with different electrolytes: (a) EMIm-TFSI; (b) MPPy-TFSI.

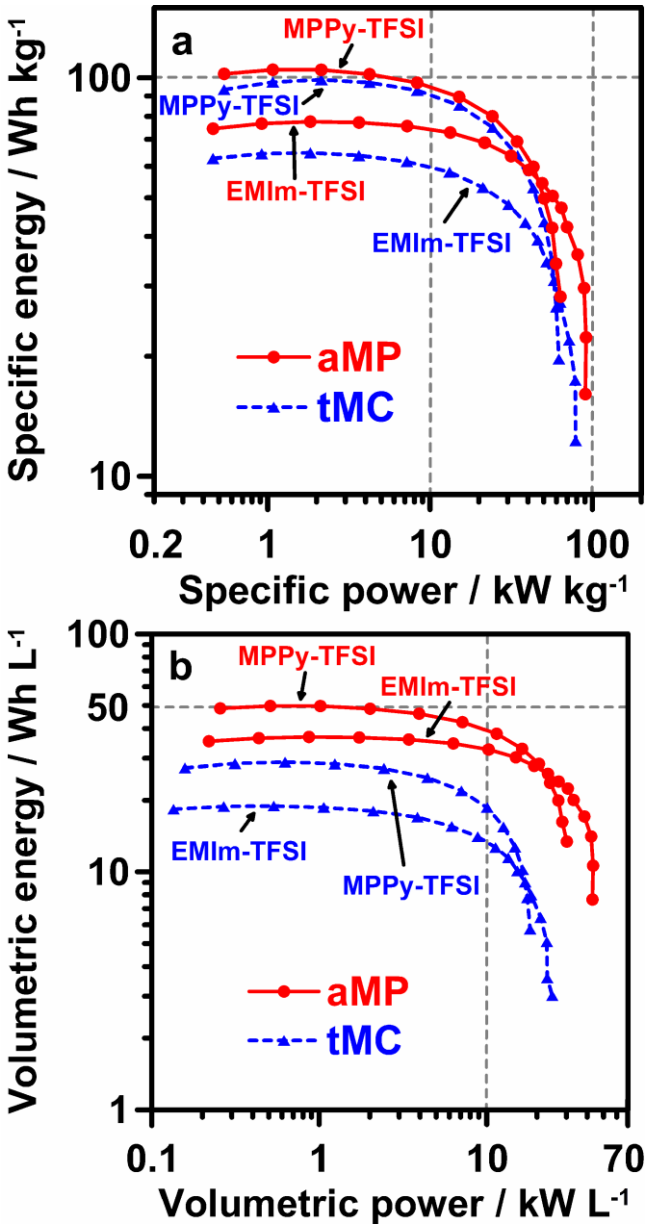

Fig. 11. Ragone plots for the aMP and tMC EDLCs assembled using EMIm-TFSI (0–3.5 V) and MPPy-TFSI (0–4 V): (a) specific energy vs. power; (b) volumetric energy vs. power.

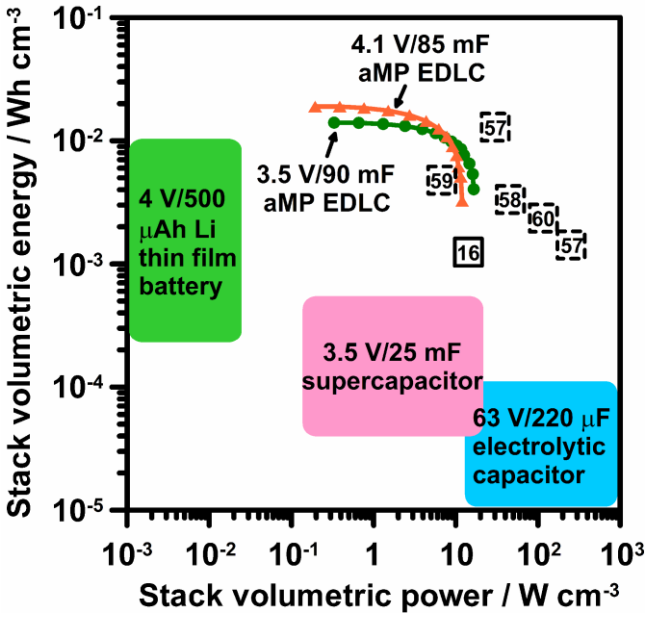

Fig. 12. Ragone plot of stack volumetric energy vs. power for the aMP EDLCs and those reported in literature and the commercially-available electrochemical devices.[16,57–60] The reference numbers of the previous studies were encompassed by squares. Reference 16 (solid square) presented conventional sandwich-type EDLCs using laser-scribed graphene electrodes. References 57–60 (dotted squares) presented micro-device electrochemical capacitors using activated carbon and onion-like carbon,[57] polypyrrole-decorated nanoporous gold,[60] laser-reduced graphene,[59] graphene-carbon nanotube carpet[60] as the electrodes.